Thermohydraulic analysis of a microchannel with varying superhydrophobic roughness

Mohammad Reza Akhtari[a,*], Nader Karimi[b]

[a]Department of Mechanical and Aerospace Engineering, Shiraz University of Technology, Shiraz 71557-13876, Iran (MR.Akhtari@sutech.ac.ir and Akhtari.MReza@gmail.com)

([*]Corresponding Author: MR.Akhtari@sutech.ac.ir)

[b]Systems Power and Energy Research Division, James Watt School of Engineering, University of Glasgow, Glasgow G12 8QQ, United Kingdom (Nader.Karimi@glasgow.ac.uk)

Abstract

Nature inspired superhydrophobic surfaces are applied to microchannels to minimize the pumping power needed for driving the fluid flow. Special attention is given to the superhydrophobic surfaces with alternative microstructures and four different micro-structured configurations including square and triangular micro-posts and micro-holes are examined in aligned and staggered patterns. A numerical study is conducted to identify the impact of cavity fractions of 0.1 to 0.9 and Reynolds numbers of 10 and 100 on the performance indicators. These include drag reduction, heat transfer rate and mixed hydraulic and thermal behavior of the microchannel evaluated by the thermal performance index. The results reveal that the Poiseuille and Nusselt numbers decrease by the increase of cavity fraction. It is also observed that the triangular patterns feature the best thermal performance. The optimal combination of heat transfer and pressure drop, reflected by the goodness factor, can be achieved in staggered square holes and posts patterns at low and high Reynolds numbers, respectively. Considering the total thermal performance of the microchannel, changing the microstructures from aligned to staggered pattern can have a significant influence upon the square micro-posts and micro-holes but only a modest impact on the triangular posts. Nonetheless, the optimal surface configuration should be picked up in accordance with the specific application in hand and by prioritizing improvements in thermal or hydraulic performance of the microchannel.

Keywords: Superhydrophobic surface (SHS); Poiseuille and Nusselt number; Slip length; Microchannel; square and triangle microstructures; goodness factor.

Nomenclature			
A	cross-sectional area of flow (m^2)	P_w	liquid perimeter

A_c	shear-free area (m^2)	$\bar{q}''$	average heat flux (W/m^2)
A_t	total wall area (m^2)	Re	Reynolds number
C_p	specific heat at constant pressure (j/kg/K)	SHS	superhydrophobic surface
D_h	hydraulic diameter (m)	T	fluid temperature (K)
f	friction factor	$\overline{T_m}$	fluid mean temperature (K)
F_c	cavity fraction	T_s	temperature of no-slip wall (K)
F_s	solid fraction	u_m	mean velocity of fluid flow (m/s)
H	microchannel height	u_s	Slip velocity (m/s)
i	x-direction component	w	solid-cavity width (m)
j	y-direction component	W_r	relative pattern width
k	fluid thermal conductivity (W/m/K)	η	thermal performance index
L	solid-cavity length (m)	λ	Slip length (m)
$MEMS$	microelectromechanical systems	μ	fluid dynamic viscosity (kg/m/s)
$\dot{m}$	mass flow rate (kg/s)	ρ	fluid density (kg/m^3)
Nu	Nusselt number	τ_w	wall shear stress (N/m^2)
Po	Poiseuille number	φ	goodness factor
Pr	Prandtl number	φ_c	smooth channel goodness factor

1. Introduction

Microdevices continue to receive a significant attention worldwide. These devices have found various applications in a number of emerging technologies including microfluidic systems, microelectromechanical technology (MEMS) and microchemical reactors. Further, microchannels are applicable in cooling of electrical devices [1] and have a high heat transfer coefficient due to their large surface to volume ratios. Microchannel can be assumed as a heat exchanger, which can be found in different types like circular tube [2,3] integrated with alternative inserts [4–6], double-layer microchannel heat sink [7], solar-based heater [8,9]. Heat transfer coefficient and shear stress increase as the hydraulic diameter of the microchannel decreases [10]. Consequently, pressure losses through microchannels are quite significant and demand a large pumping power, which is clearly a major drawback.

To address this issue, employing nature inspired superhydrophobic surfaces (SHSs) found on a lotus, rice leaf, butterfly wings, lizard skin, collembolan, shark skin, fish scale, red rose petal, poplar leaf [11], appeared to have a significant potential. On SHSs, the contact angle of droplet transgresses 150°, which could be made by capillary coatings, spray coating, chemical etching, solution immersion, laser electrodeposition, sol-gel, atmospheric pressure plasma, photolithography and colloidal assemblies [12,13]. It is worth mentioning that SHSs have a large number of applications including producing self-cleaning, anti-icing, anti-corrosion [14], anti-fouling, anti-reflective [15] and anti-fogging surfaces as well as liquid transport and separation [16], water collection and biomedical applications [17]. These have turned SHSs into an exciting and largely unexplored research topic.

1.1. Literature review

Drag and friction can often cause major engineering challenges. Shear stress is responsible for about 50% of drag on ships [18] and leads to consumption of a large amount of energy in industrial processes. Water is considerably utilized to transfer waste thermal energy to the environment [19]. On SHSs, air is trapped between nano/microstructures and due to surface tension and their small size, water infiltration into micro holes is not possible. This constitutes a shear-free air-water interface and therefore reduces the flow friction. This state is known as Cassie-Baxter [20], where liquid droplets remain at the top of roughness. Alternatively, liquid droplet penetrates the microstructure and lead to Wenzel's state [21]. Ou et al. [22] carried out an experiment and reported the pressure drop and slip length for SHS with the cavity fractions in access of 0.95. As solid-water interface (wetted contact area) decreases, a drop in the pressure loss and a convenient fluid flow through microchannels becomes achievable [23].

A large number of investigations have been already carried out on various SHS structures, flow and boundary conditions. Maynes et al. [24] analyzed longitudinal rib and cavity walls in microchannels with laminar flow analytically. Teo and Khoo [25] as well as Cowley et al. [26] examined this phenomenon with transverse grooves and square pillars, respectively. Haghighi et al. [27] explored the effect of superhydrophobicity on the axial hydraulic turbine by entropy generation method. Krishnan et al. [28] observed the improvement of 97% in heat flux and 88% in heat transfer coefficient by silane coating of picosecond laser-treated SHS. Another interesting study indicated that air conditioner efficiency could be enhanced by using SHSs in heat exchanger [29].

Choi et al. [30] revealed that trapped air between grooves could be depleted by high-pressure gradient although this issue can be addressed by cutting down the length and width of the cavities. In Norouzi et al. [31] study, the maximum drag reduction was attainable when the fluorocarbon compound as a water repellent was used on the pre-treated surface. This is because of the creation of microbubbles between substrate and water flow that leads to water slippery over the surface and thus more reduction in drag. Tuo et al. [32] fabricated anisotropic SHS on stainless steel comprising inclined grooves by laser etching and fluoride treating for drag test. Comparing inclined and reversed direction of ribs, while drag-drop ratio in the first situation is about 18%, it is almost 48% in the latter under 4.48m/s flow velocity. Tuo et al. [33] used aluminum foil and one-step hydrothermal mechanism to prepare their SHS by $Al[CF_3(CF_2)_{12}COO]_3$ with small sliding angle and huge contact angle resulting in almost 20-30% drag reduction at 2-5m/s fluid velocity.

Considering turbulent flows, Rastegari and Akhavan [34] conducted a numerical work on high Reynolds number flows in which they investigated drag reduction of micro-posts and micrograms aligned with flow direction. They observed that drag reduction and the sustainability bounds of SHS deteriorate as the Reynolds number increases. Rajappan et al. [35], found that for a turbulent flow, small surface roughness, a large autocorrelation length as well as hierarchical roughness are necessary to achieve excellent drag reduction along with having a Cassie-Baxter state [36]. Also, these authors pointed out that to overcome the depletion of air trapped among microstructures, as a necessity for superhydrophobicity maintenance, further investigations should be carried out in turbulent flows and their feasibility. However, some strategies have been under investigation to tackle this issue. Gose et al. [37] showed that for reaching the desired drag reductions in turbulent flows, surface roughness and the contact angle hysteresis (CAH) should be minimized. In their study, 50% reduction in drag was achieved in high-velocity turbulent flows like those related to naval applications. Moreover, a higher heat transfer can be reach by using alternative working fluid like nanofluids [38].

1.2. Objectives

The review of literature revealed that there is an extensive room to produce commercial and sustainable SHSs for diverse applications. Some durable and cost-effective SHSs prepared with advanced methods have been tested for certain purposes targeting mechanical or chemical fabrication process, anti-corrosive, anti-icing, anti-fungal, anti-fogging or self-cleaning surfaces, which are worth examining in other applications. This approach has addressed a wide range of technical issues in many fields ranging from daily life to industry and medicine. Importantly, some kinds of SHSs seem to be durable and applicable in one area but fail in other functions. This sensitivity calls for careful experimental and numerical analyses before mass production of such surfaces. There have been extensive investigations on SHSs comprising micro-posts [39–41], micro-holes [42], transverse [25,43] or longitudinal (streamwise) ribs and cavities [24,44,45] produced physically or chemically. Each of them focuses on a particular aspect of fluid flow over SHSs such as friction factor, slip and temperature jump length. However, investigations on other geometries have, so far, received much less attention. From which, triangular patterns have drawn few thermal and hydraulic considerations.

Augmentation of heat transfer has been the focus of a number of studies including the recent work of Ryu et al. [46] on improvement of heat transfer by microstructures. The promising heat removal effect of SHS with aligned micro-posts in microchannels comparing with that of conventional microchannels was shown by Cheng et al. [47]. They also indicated that the Nusselt number rises by accelerating and decelerating the flow through the microchannel. Taking advantage of different types of roughness could make the flow acceleration and deceleration achievable. Further, staggering the roughness can be seen as a viable route to reaching higher Nusselt numbers, as the flow experiences more acceleration and deceleration, while there is an almost little frictional resistance. In the current study, it is attempted to carry out numerical work on the role of SHSs in drag reduction and heat transfer within microchannels. To show the superiority of the proposed SHSs, the results on Poiseuille and Nusselt number as well as the total thermal index are compared to those of conventional surfaces. The survey of literature revealed that, so far, little attention has been paid to alternative roughness and especially to the staggered triangular microstructure. Therefore, the proposed microstructures are SHSs with square and triangular micropillars and micro-holes. This study aims to broaden the current horizons in adoption of SHSs to overcome commercial and industrial barriers. Finally, even though SHSs are examined for drag reduction and heat transfer, their other advantages should not be overlooked. These include being self-cleaner, anti-corrosive, anti-fouling and so on, which foster further research to exploit these versatile SHSs.

2. Methodology

SHSs with four different microstructures, namely square and triangular micro-holes and micro-posts on a lattice, are employed to investigate drag reduction and heat transfer in a microchannel. The proposed geometries and mesh were generated in ANSYS Gambit 2.4.6. The schematics of the aligned and staggered roughness are depicted in Fig.

1. Due to symmetry, only half of the height of microchannel ($H/2$) was simulated. Fig. 2 illustrates the computational domains in dotted and solid lines with width of W, length of L (equal to W for square patterns) and the relative pattern width can be defined as $W_r = W/D_h$. The hydraulic diameter ($D_h = 4A/P_w$) can be equated to $2H$ considering an infinite width of microchannel, where A and P_w denote flow cross area and fluid perimeter, respectively.

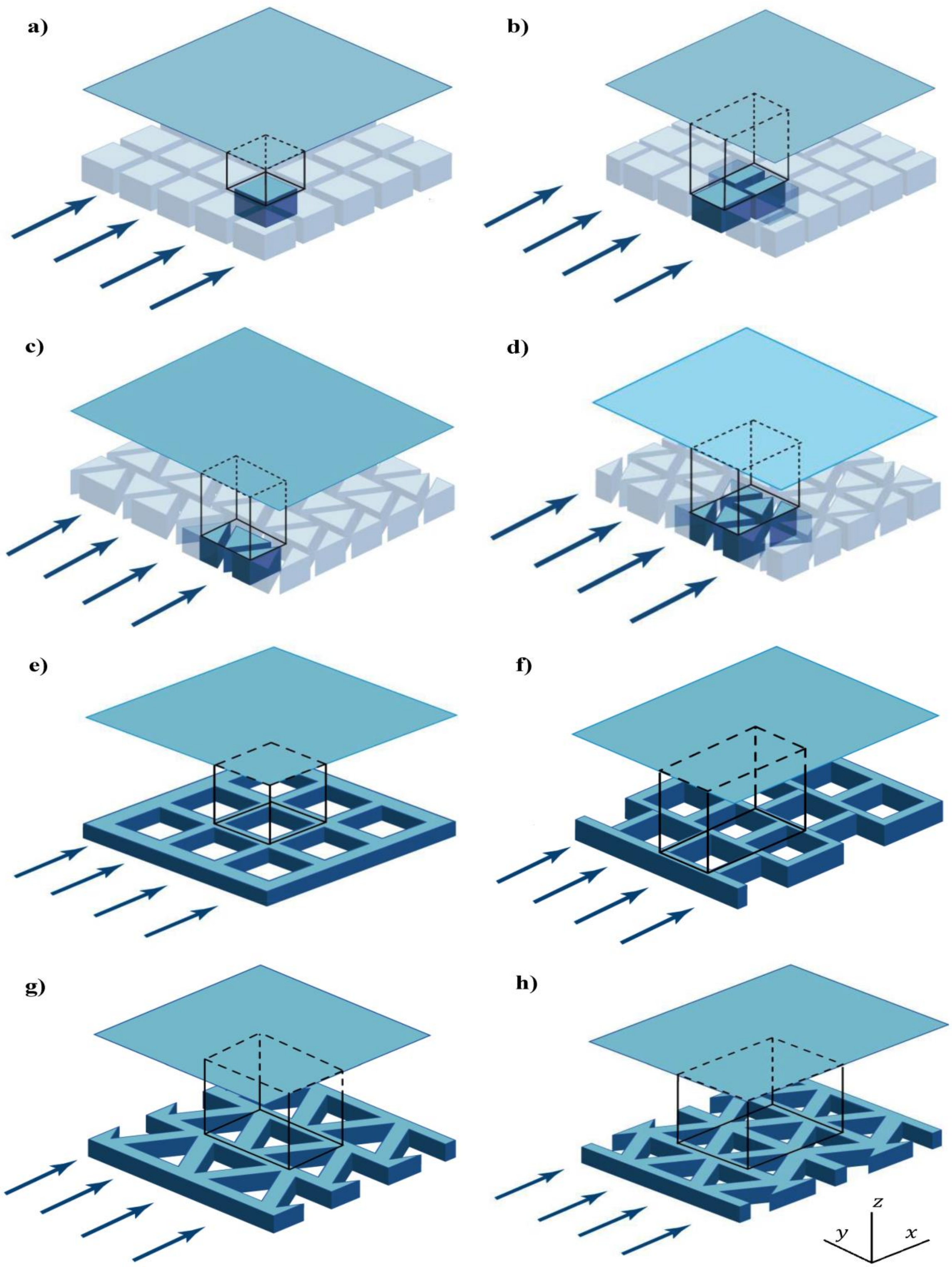

Fig. 1. SHSs microstructures a) aligned square micro-posts, b) staggered square micro-posts, c) aligned triangular micro-posts, d) staggered triangular micro-posts, e) aligned square micro-holes, f) staggered square micro-holes, g) aligned triangular micro-holes and h) staggered triangular micro-holes. Fluid flow is shown with arrows and symmetric plane by the upper surfaces.

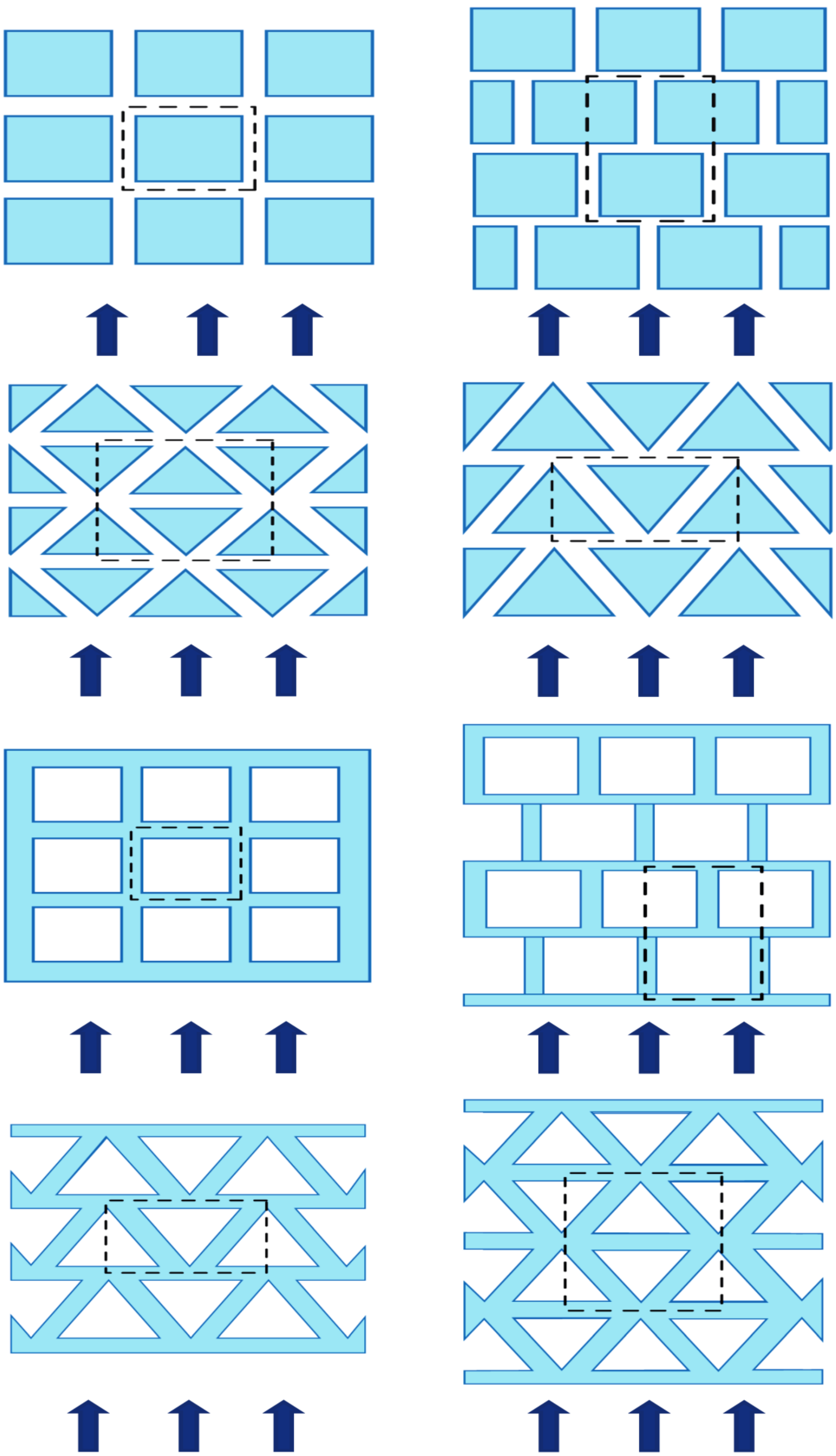

Fig. 2. Top view of SHSs for different patterns with flow direction and computational domain. Each domain has a width of W.

Cavity fraction and Reynolds number are defined as $F_c = A_c/A_t$ and $Re = \rho\overline{u_m}D_h/\mu$, where A_c, A_t, $\overline{u_m}$, ρ and μ are the cavity area, surface area of the microchannel wall, mean fluid velocity, fluid density and dynamic viscosity, respectively. To identify the effect of SHSs with various microstructures on the pressure drop and heat transfer through the microchannel, Poiseuille number and Nusselt number were investigated. These are constant in conventional channels with fully developed laminar and incompressible flows. The production of friction factor and Reynolds number lead to Poiseuille number ($Po = fRe$) and will be evaluated in a few cases to represent the strength of different geometries on drag reduction. Friction is deemed to be a serious issue hindering fluid flow in micro/nanodevices, and therefore should be addressed effectively to reduce pumping energy. The friction factor is defined as

$$f = 8\,\overline{\tau_w}/\rho\bar{u}_m^2, \tag{1}$$

where $\overline{\tau_w}$ and ρ are the average wall shear stress and fluid density. Slip length, defined as the normal distance from wall to where streamwise velocity diminish, can be calculated in terms of gradient of fluid velocity l and slip velocity on the channel wall by [48]:

$$\lambda = \frac{u_s}{\left(\frac{\partial u}{\partial z}\right)}. \tag{2}$$

To evaluate the thermal performance of SHSs, the proposed formula for Nussle number by Enright1 et al. [49] can be used. This reads:

$$Nu = \frac{\bar{q}''D_h}{k(\overline{T_s}-\overline{T_m})}, \tag{3}$$

in which k is the fluid thermal conductivity, $\bar{q}''$ is the average heat flux imposed on the microchannel wall, $\overline{T_s}$ is the mean temperature of no-slip (solid) part of SHS and $\overline{T_m}$ is the average temperature of the fluid through the microchannel. The local friction factor and Nusselt number can be represented at each point as:

$$f_x = 8\,\overline{\tau_{w,x}}/\rho\bar{u}_m^2, \tag{4}$$

and

$$Nu_x = \frac{\bar{q}_x''D_h}{k(\overline{T_{s,x}}-\overline{T_{m,x}})}. \tag{5}$$

Maynes et al. [24] showed that the effect of meniscus angles is just less than 4% for fully developed laminar flow in microchannel. Therefore, the solid-liquid interface assumed to be due to the trivial amount of difference between viscous and surface tension forces [47]. On the basis of the existing theories, the supportable pressure by air-water interface could be calculated by Young's law [50]. As the cavities and distances between posts are in the order of micro-meter and microchannels with SHS experience less frictional resistance, the Cassie state [51] is considered here. This expresses that with the help of surface tension the liquid does not penetrate into the cavities [40]. Further, since liquid penetration into the cavities depends upon various factors such as manufacturing methods and quality, type of materials, liquid surface tension and flow pressure, new methods have been proposed to increase the superhydrophobicity of the surfaces and liquid-air durability [52–54]. For example, Carlborg et al. [55] showed that air pockets on a modified surface could support liquid pressures that are three times higher than the theoretical predictions. Further, as mentioned earlier, a cavity fraction of more than 0.95 was studied experimentally [22], the maximum cavity fraction is considered to be 0.9 in the current study. Although the maximum amount of pressure drop is less than 5 kPa and the supportable pressure by air-water interface could be calculated by Young's law [50], Samaha et al. [53] were able to reach proper drag reduction under the hydrostatic pressure of 600 kPa.

2.1. Numerical method

To evaluate the effect of different geometries and patterns, five cavity fractions of 0.1, 0.3, 0.5, 0.7 and 0.9 under incompressible and laminar flow with Reynolds numbers of 10 and 100 are considered. Hydraulic diameter is 1 mm, relative pattern width is 1, inlet flow temperature is 300 K and constant wall heat flux justified to be $70000\ \mathrm{W/m^2}$. The Nusselt number is independent of the amount of heat flux and it is just a function of cavity fraction [49] and is selected to be small enough to prevent water boiling at the outlet of the microchannel. The width and length of the computational domain for square posts will be 1 × 1 mm and for triangular posts is 1 × 0.866 mm with the same height of 0.25 mm. Constant surface heat flux is applied on the no-slip (solid) part of SHS and is small enough for fluid flow to prevent reaching saturation temperature. The cavity-liquid interface assumed to be adiabatic and shear free (slip condition) surface. The finite-volume approach by ANSYS Fluent 6.3.26 was utilized for numerical solution of fluid flow and heat transfer in microchannel. Considering discretization of momentum and energy equations, the second order upwind method was employed along with SIMPLEC algorithm for the pressure-velocity coupling.

2.2. Governing equations and boundary conditions

Water is considered as the working liquid. Considering constant properties ($\rho = 998.2\ \mathrm{kg/m^3},\ \mu = 0.001003\ \mathrm{kg/\frac{m}{s}},\ k = 0.6\ \mathrm{W/m/K}\ and\ C_p = 4180\ \mathrm{J/kg/K}$) and being an incompressible, the following equations are solved.

Continuity of mass:

$$\frac{\partial(u_i)}{\partial x_i} = 0. \tag{6}$$

Transport of fluid momentum in three dimensions:

$$\rho\frac{\partial(u_i u_j)}{\partial x_i} = \mu\frac{\partial}{\partial x_i}\left(\frac{\partial u_j}{\partial x_i}\right) - \frac{\partial p}{\partial x_j}, \tag{7}$$

and transport of fluid energy:

$$\frac{\partial(u_i T)}{\partial x_i} = \frac{k}{\rho C_p}\frac{\partial}{\partial x_i}\left(\frac{\partial T}{\partial x_i}\right). \tag{8}$$

In Eqs. (5-7), fluid viscosity, thermal conductivity, specific heat at constant pressure, fluid temperature, component of flow velocity in direction of x and pressure are denoted by μ, k, C_p, T, u_i and p, respectively.

As there are translationally periodic geometries, the inlet / outlet and sides of the computational domain are defined as periodic boundaries for all cases. To validate this boundary condition, the complete lengths of the microchannels were simulated for some cases and the results showed a good agreement with periodic inlet/outlet boundary condition for both Nu and fRe. Symmetry boundary was applied to the above surface at the height of $H/2$ due to facing the symmetry conditions in the current study. The solid portion with no-slip condition and air-packed region with free-shear stress are depicted in Fig. 3 for the aligned and staggered square micro-posts. The red portions indicate the solid part of liquid-solid interface with constant heat flux. The remaining areas are air-liquid interface assumed to be adiabatic as a result of small thermal conductivity of air in comparison with water. To ensure acceptability of the results and convergence, the simulations were regarded as converged with the residuals being less than 10^{-8}. Fluid flow with specific Reynolds number within the microchannel was achievable by applying pressure gradient and mass flow rate on the inlet and outlet periodic boundary conditions. The desirable mass flow rate can be calculated by the mean velocity of fluid flow ($\overline{u_m} = Re\mu/\rho D_h$) through the cross-section area of microchannel (A) at $Re = 10$ and 100 by:

$$\dot{m} = \rho A \overline{u_m} \tag{9}$$

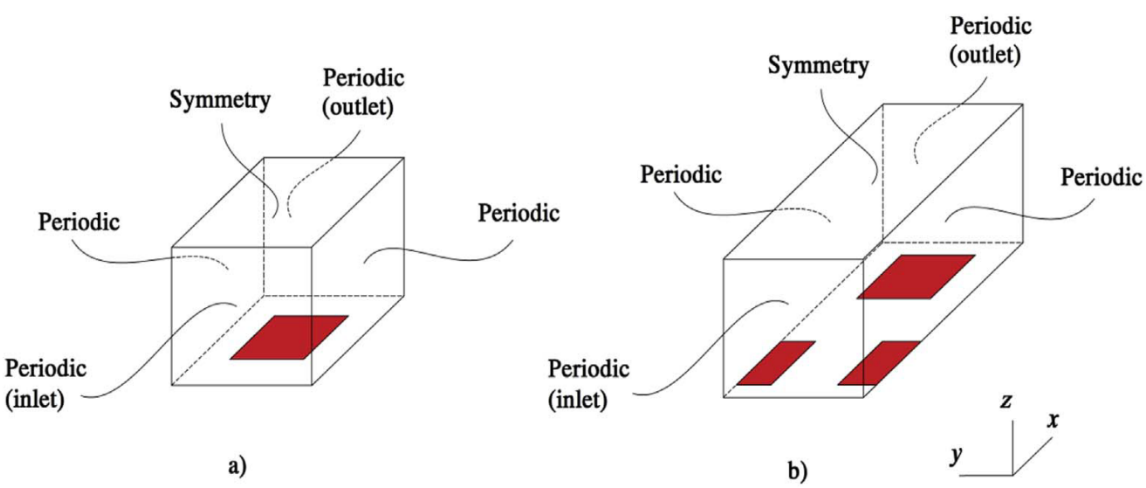

Fig. 3. Computational domains for a) aligned square micro-post b) staggered square micro-post.

The top and right views of the computational domain are also represented in Fig. 4 for aligned and staggered square micro-posts. The computational domains are demonstrated in dark areas.

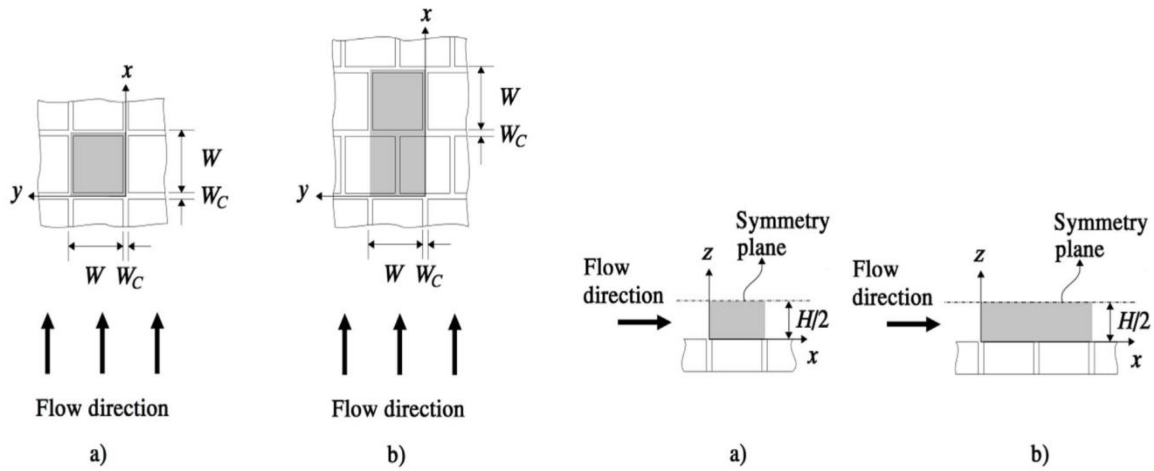

Fig. 4. Top and right views for a) aligned b) staggered square micro-post. Grey areas illustrate the computational domain.

2.3. Grid independency and validation

A structured grid was generated for microchannels with square posts and holes and a hexa mesh for triangular part of the microchannels with triangular micro-posts and micro-holes. The concentrated grids were adopted near the edges due to the high variation in fluid flow. The grid independency study was carried out using refined and coarse meshes under Reynolds number of 100 at cavity fraction of 0.1 and 0.9, where the strongest gradients occur, to compare the values of Poiseuille and Nusselt number for all geometries.

To illustrate structure of the generated grid, Fig. 5 presents the coarse grid for aligned and staggered square patterns of micro-posts at cavity fraction of 0.9. The surface of solid portions of SHS are at the opposite side of the red portions of symmetry plane at the lowest part of the computational domain. Table 1 shows the results of grid independency study for the aligned and staggered micro-posts and at Reynolds number of 100 and cavity fractions of 0.1 and 0.9, respectively. This suggested that the coarse grid offers acceptable results with just less than 3% differences with the refined mesh for both aligned and staggered configurations. The adopted grid size in the x, y and z directions for the square patterns are 60 × 60 × 13 and 118 × 92 × 15, and for triangular patterns are 64 × 46 × 13 and 64 × 92 × 13 in the aligned and staggered configurations, respectively.

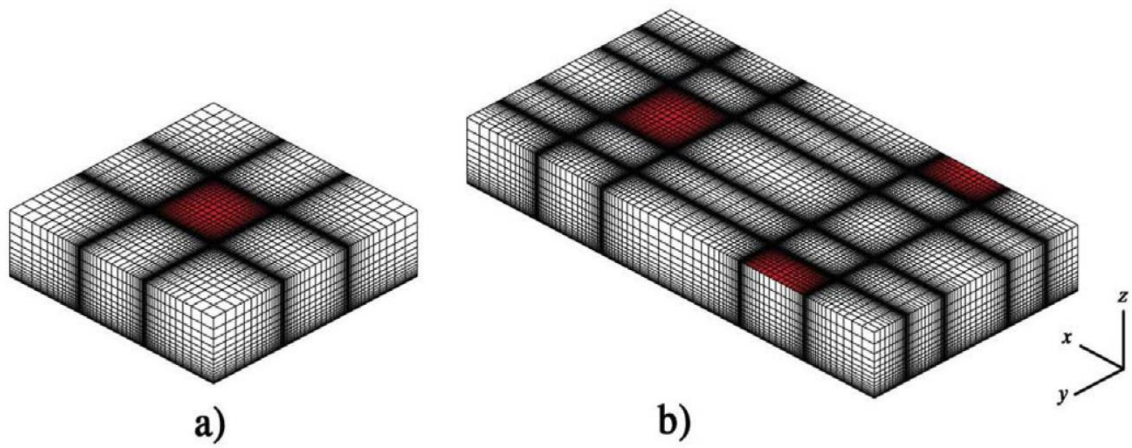

Fig. 5. Coarse grid utilized for grid study at $F_c = 0.1$. a) aligned b) staggered square micro-post.

Table 1

The Poiseuille and Nusselt numbers of aligned and staggered patterns of micro-post for the refined and coarse grids at Reynolds number of 100 and $F_c = 0.1$.

	Aligned				Staggered			
	Refine		Coarse		Refine		Coarse	
	Po	Nu	Po	Nu	Po	Nu	Po	Nu
Square post	93.9	8.02	93.3	7.99	93.9	8.08	93.4	8.05
Square hole	91.5	7.8	90.9	7.86	91.1	8.03	91	8.03
Triangular posts	91.1	8.11	93.9	8.11	94.3	8.1	93.9	8.1
Triangular holes	92	8.02	91.98	8.03	92.3	8.02	92	8.03

Table 2

The Poiseuille and Nusselt numbers of aligned and staggered patterns of micro-post for the refined and coarse grids at Reynolds number of 100 and $F_c = 0.9$.

	Aligned				Staggered			
	Refine		Coarse		Refine		Coarse	
	Po	Nu	Po	Nu	Po	Nu	Po	Nu
Square post	14	1.55	13.8	1.54	18.6	2.64	18.3	2.6
Square hole	29	2.67	28.9	2.71	30.2	47	29.8	3.51
Triangular posts	22.7	2.87	22.5	2.88	22.6	2.83	22.4	2.9
Triangular holes	38.7	5.28	37.3	5.27	38.4	4.91	37	5.03

As mentioned earlier, Enright et al. [49] developed an analytical solution for the Nusselt and Poiseuille numbers in microchannels (among two parallel plates extended to infinity) with aligned square micro-post. Their solution is a function of the thermal and hydrodynamic slip length on the channel wall. This was obtained under some conditions that are valid for solid fraction ($F_s = A_{solid}/A_{wall}$) less than 0.9, where the diffusive heat transfer is dominant at creeping flow near SHS ($Re_w = \rho W \widetilde{u_w}/\mu \rightarrow 0$). Therefore, the numerical solutions were validated for $Re = 10$ and relative pattern width of 0.01, where the low amount of Re_w was accessible through the performed numerical study. Fig. 6 demonstrates a good agreement between the outcomes of the current numerical simulations and those of the analytic work of Enright et al. [49]. This agreement confirms capability of the current numerical simulations in analyzing laminar fluid flows with different patterns of microstructures.

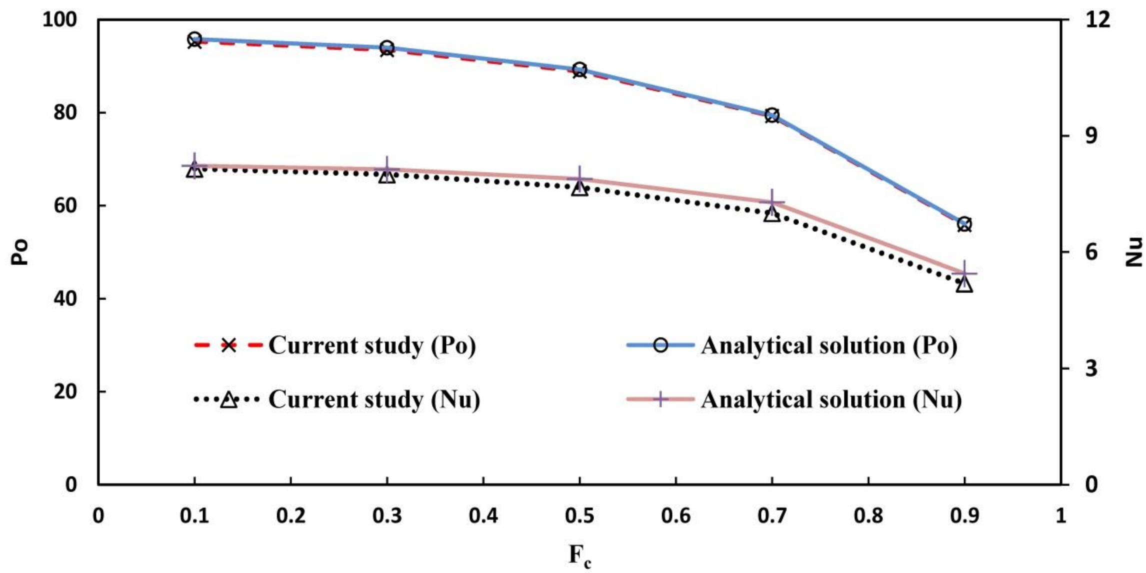

Fig. 6. Comparison between the Nusselt and Poiseuille numbers obtained from the numerical and theoretical approaches [49].

3. Results and discussion

In this section, diverse parameters are calculated numerically for four various patterns on SHS to analyze the effects of different geometries on drag reduction and heat transfer within the microchannel. Then, the total performance of SHS on simultaneous drag reduction and heat transfer enhancement will be discussed in the context of goodness factor.

3.1. Drag reduction

Fig. 7 represents Poiseuille number versus different cavity fractions at Reynolds number of 10 and 100 for aligned and staggered patterns of microstructures. As can be seen, the Poiseuille number approaches 96 (an amount of Po in conventional channels) as the cavity fraction becomes smaller. Shear free interface increases as the cavity fraction rises from 0.1 to 0.9 resulting in lesser friction resistance on the microchannel walls. Consequently, the value of Po drops indicating the smallest amount of pressure drop in microchannels at $F_c = 0.9$. It can be seen that in low and high cavity fractions, SHS with aligned square holes and posts can impose a great effect on pressure drop through microchannel, respectively. However, the differences between Po in staggered and aligned patterns are negligible at low cavity fraction and become more distinctive as the surface cavity increases. This phenomenon can be also demonstrated by ramping up the hydraulic slip length on the SHS as the cavity fraction steps up (Fig. 8) and the fluid flows a longer distance without experiencing wall shear stress.

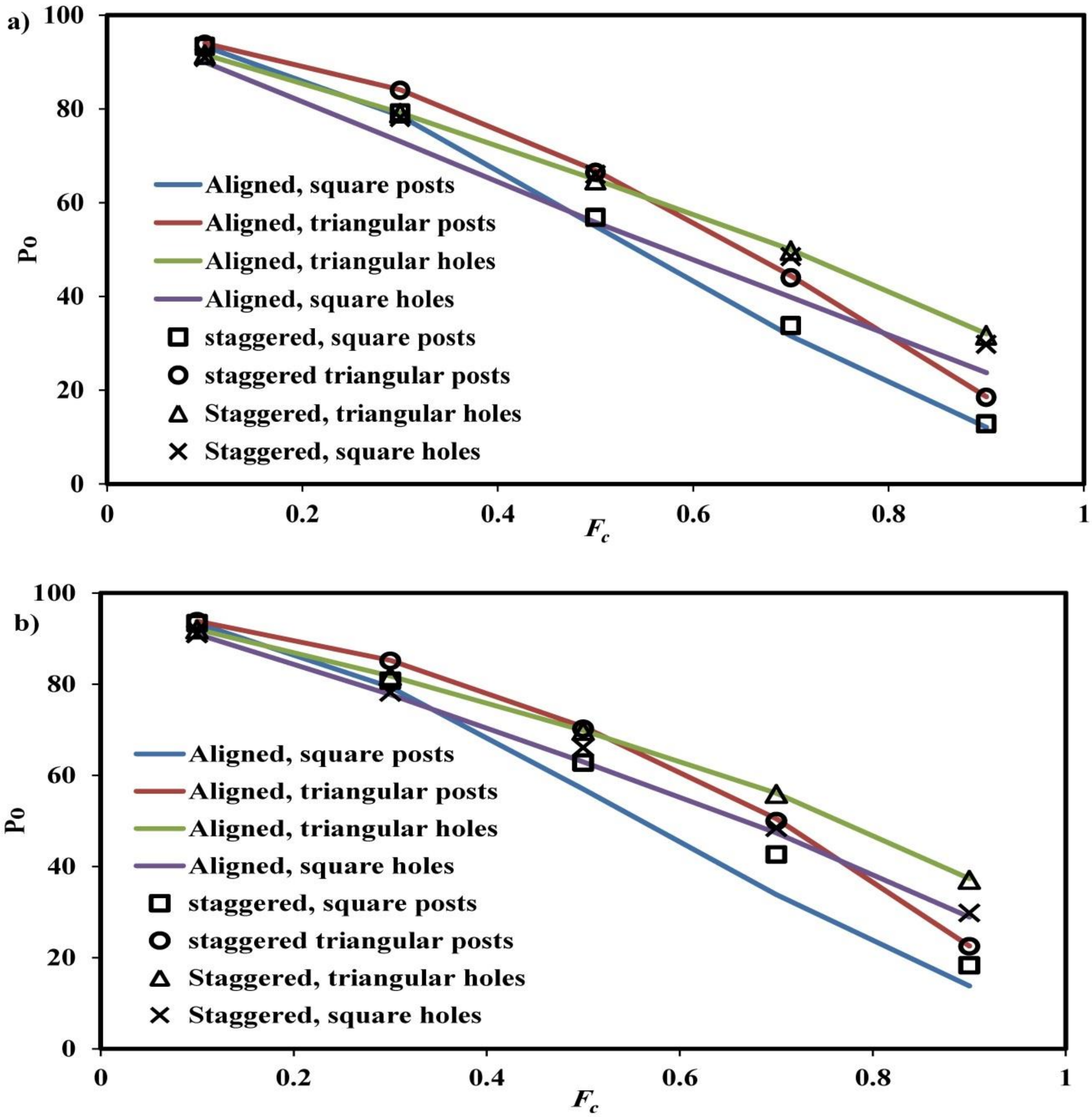

Fig. 7. Impact of cavity fraction on the Poiseuille number for different patterns at a) $Re = 10$ b) $Re = 100$.

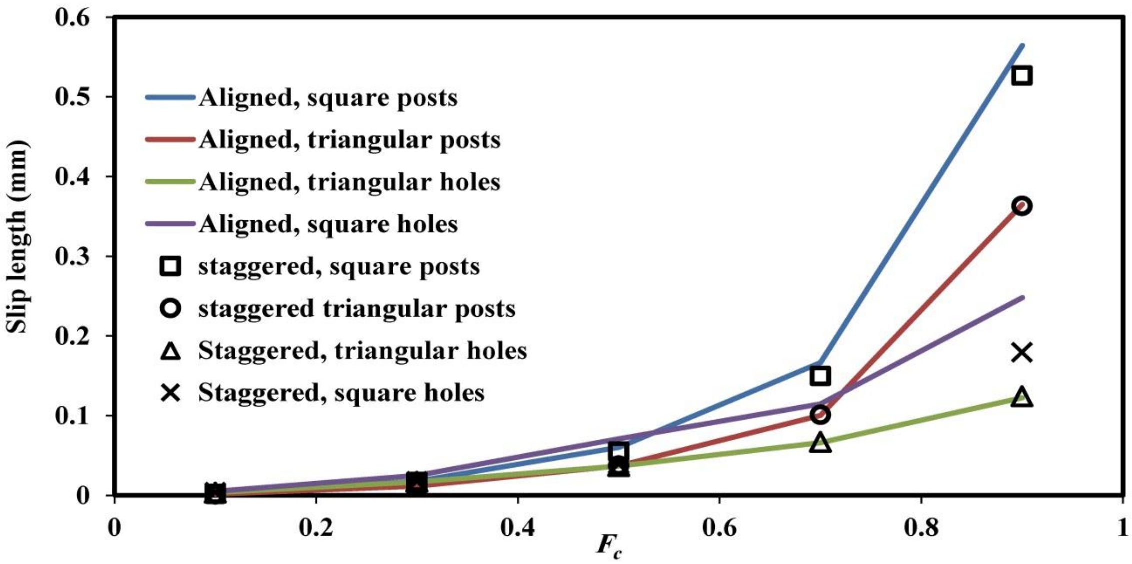

Fig. 8. The effect of cavity fraction on the slip length at $Re = 10$.

Although the overall wall shear stress declines by the increment of cavity fraction, the local amount of this parameter enhances as the acceleration and deceleration of particles become notable at the entering and leaving edges of the microstructures. The local distribution of wall shear stress along the flow direction is illustrated in Fig. 9 for different cavity fractions and geometries versus non-dimensionalized microchannel length for a) square and b) triangular patterns at Re $= 100$. As the graphs show, generally, the maximum amount of local shear stress occurs at $F_c = 0.9$ for square micro-holes and triangular micro-post in aligned pattern. Nonetheless, the highest value of average surface shear stress on the SHS can be seen at $F_c = 0.1$ due to the dominancy of no-slip wall to cavity area. Thereupon, the Poiseuille number within the microchannel declines by the rise of cavity fraction in all cases as the slip-boundaries grow. Considering staggered microposts, fluid particles pass the longer way than aligned patterns when they depart a post to the adjacent one, which consequently leads to a higher velocity and stronger local shear stress. However, these passage lengths in the triangular patterns are almost the same and the differences in local shear stress are negligible (Fig. 12).

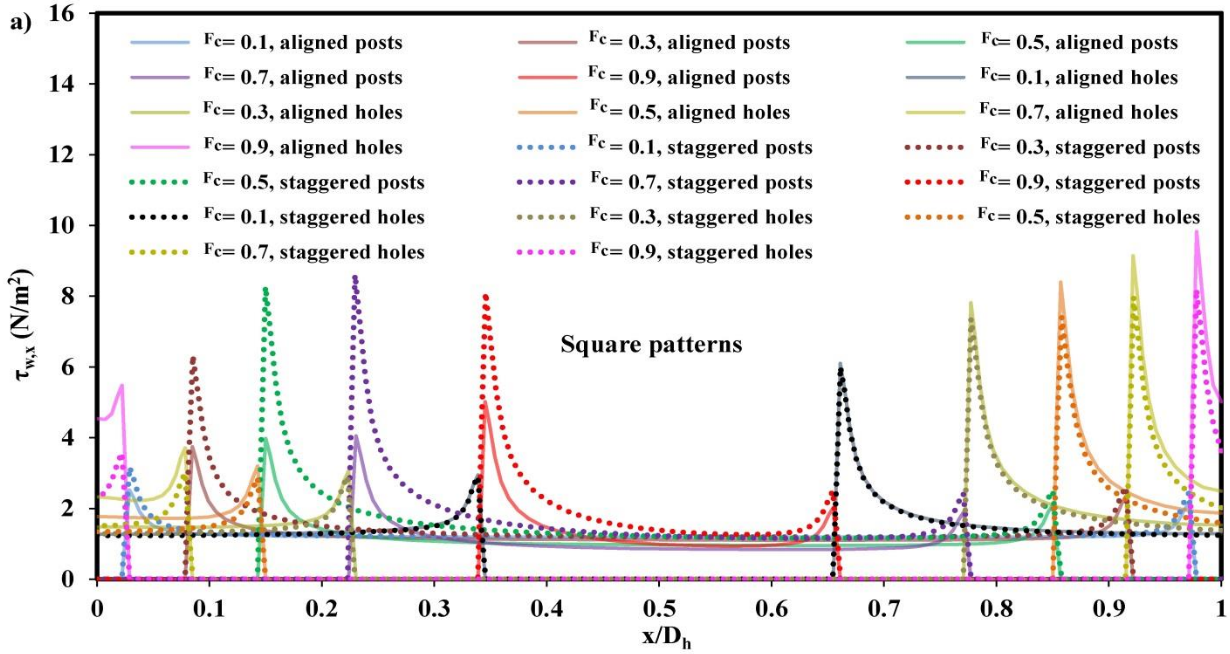

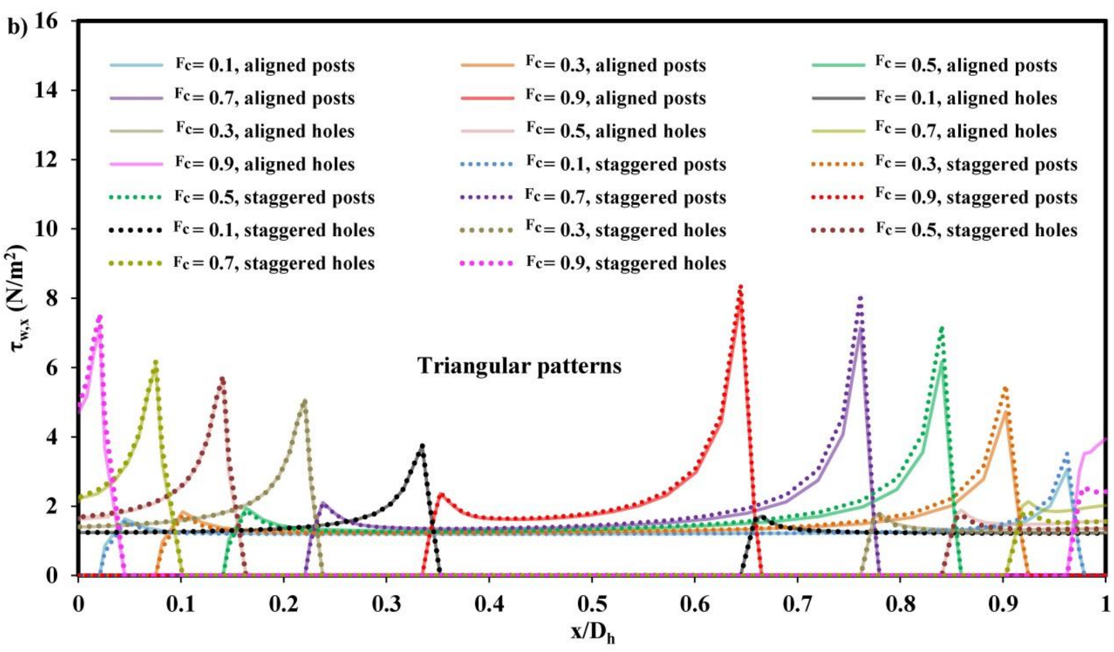

Fig. 9. Local wall shear stress versus various cavity fractions for a) square and b) triangular patterns at $Re = 100$. Solid lines denote aligned and dotted lines denote staggered configurations.

3.2. Heat transfer

Nusselt number fluctuations against cavity fraction are represented for different patterns in Fig. 10a for $Re = 10$ and Fig. 10b for $Re = 100$. The Nusselt number tends to reach the value of 8.235 in conventional microchannel with constant wall heat flux at the lowest cavity fraction. It can be realized that SHS have an adverse effect on the overall thermal performance of the microchannel. However, the local Nusselt number increases as the cavity fraction rises. The values of local Nusselt number are demonstrated in Fig. 11 for different patterns at $Re = 100$ and $F_c = 0.5$. The results show that the minimum and maximum values of the local Nusselt number occur at the aligned square micro-posts and micro-holes, respectively.

The Nusselt number also increases by the rise of Reynolds number. Fig. 12 demonstrates this impact on the different superhydrophobic patterns. This figure indicates that the aligned triangular posts and holes pattern have the best heat transfer performance at low and high cavity fractions for all Re. However, aligned square holes and posts depict the worst performance at small and massive cavity fraction at all Reynolds numbers. Further, square configurations take advantage of being staggered in terms of thermal performance while it makes negligible differences for triangular patterns.

Staggered configurations bring about enhanced Nusselt number for square patterns but have a detrimental impact on the triangular configurations. This is due to the fact that in staggered square posts, working fluid passes the long distance before confronting the adjacent posts leading to higher velocity of particles and thinner thermal boundary layer. Regarding square holes, displacing the microstructures results in the smaller passage of particles over the solid surfaces and increase of thermal performance accordingly.

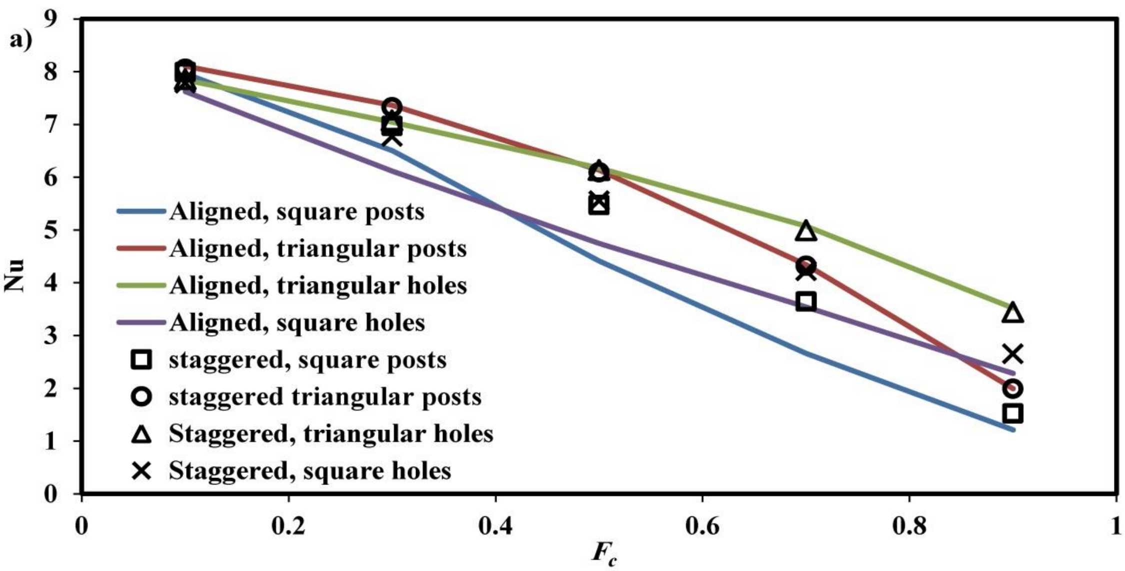

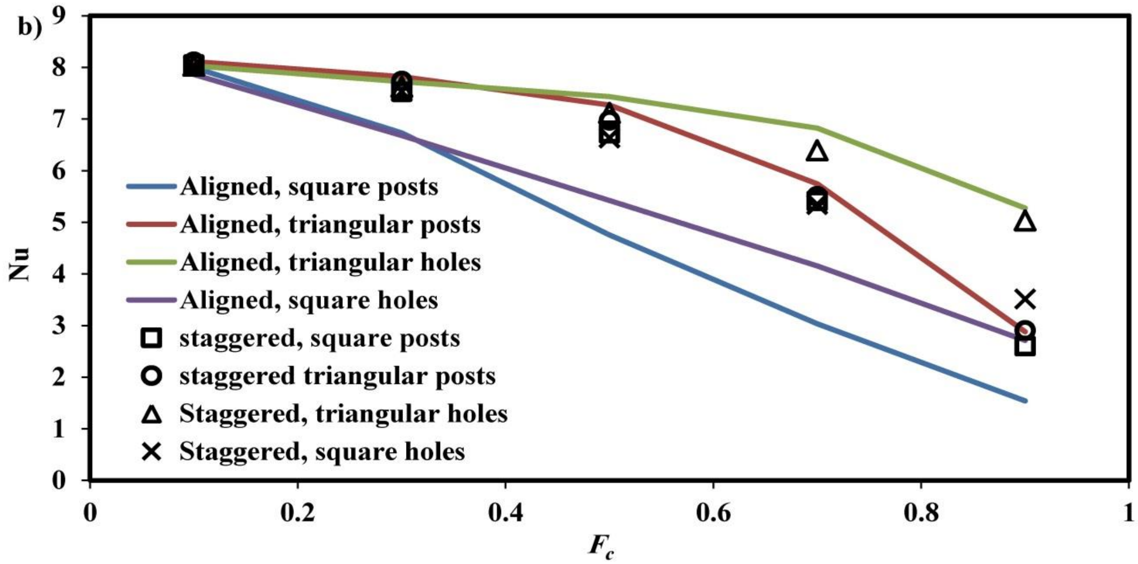

Fig. 10. The effect of cavity fraction on the Nusselt number for different patterns at a) $Re = 10$ b) $Re = 100$.

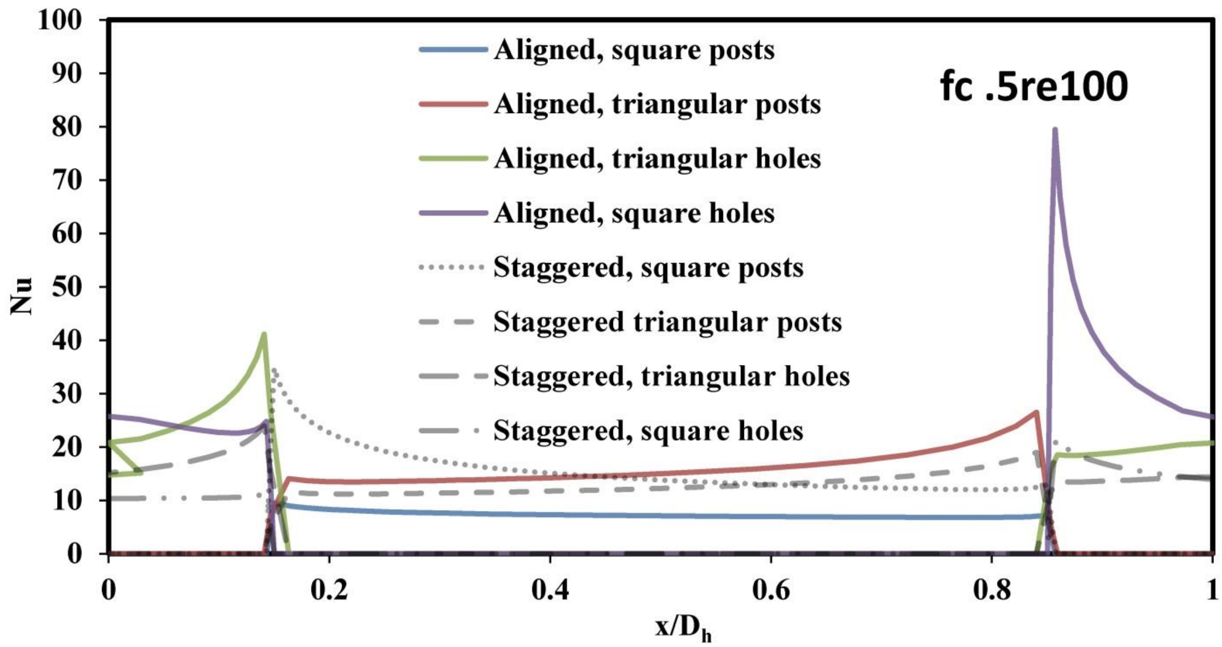

Fig. 11. Comparison of the local Nusselt numbers for different patterns at $Re = 100$ and $F_c = 0.5$.

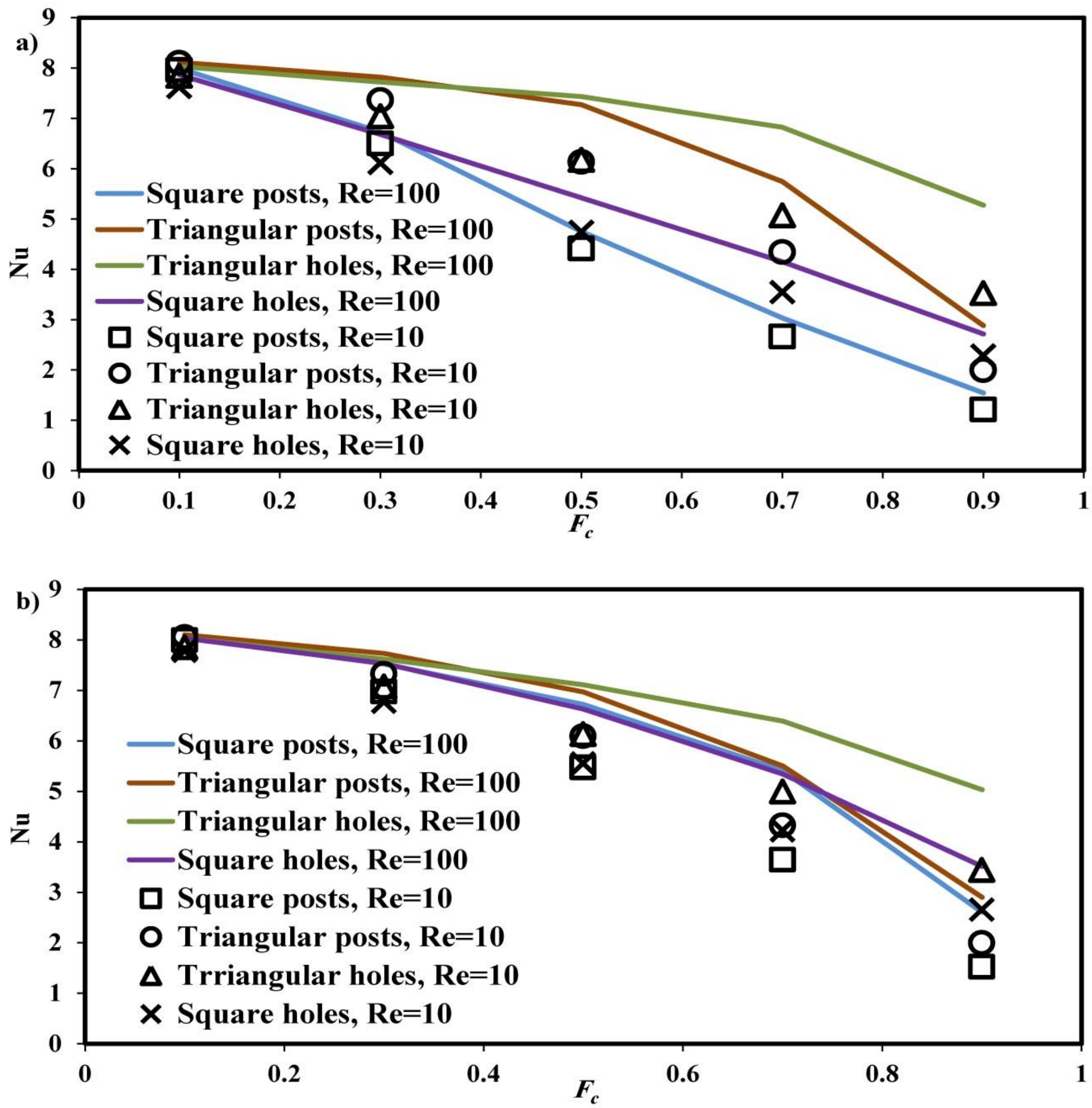

Fig. 12. Impact of Reynolds number on the Nusselt number at various cavity fractions for a) aligned and b) staggered patterns.

Fig. 13 depicts the contour of velocity magnitude over microchannel wall for diverse patterns at Reynolds number of 100 and cavity fraction of 0.5. As can be seen in square micro-posts, a part of fluid flow is always over shear—free interface resulting in higher pressure drop through the microchannel and lower Nusselt number. However, in staggered configuration, heat transfer is superior due to the thinner thermal boundary layer as the fluid particles pass the long distance over no-shear interface and speed up. Likewise, considering aligned square micro-holes, a part of fluid is always in contact with the solid section leading to the low pressure drop, thicker thermal boundary layer and consequently lower convective heat transfer through SHS than that of staggered configuration.

In sharp contrast to the situation encountered in micro-holes, the heat transfer in SHS comprising aligned triangular micro-posts is stronger than that of staggered one. This is because the fluid particles confronting the cavity-solid and only solid interface after leaving trailing edge of triangular micro-posts in aligned and staggered configurations, respectively. As triangular micro-holes are concerned, fraction of the fluid flow over solid interface in staggered patterns is more than that over the aligned configuration. This behavior leads to enhanced heat transfer in aligned triangular micro-holes.

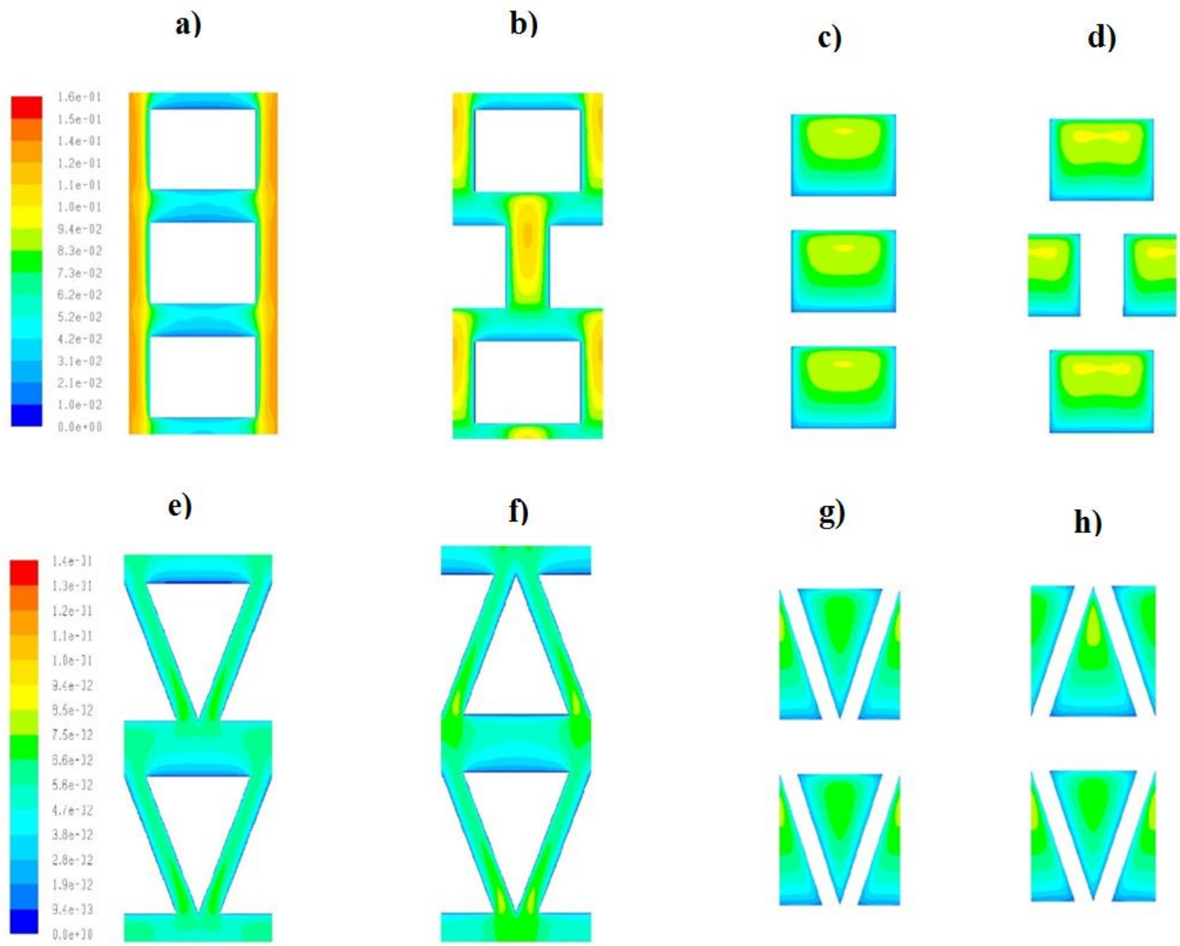

Fig. 13. Velocity magnitude contour at $Re = 100$ and $F_c = 0.5$ for a) aligned and b) staggered square micro-posts, and c) aligned d) staggered square micro-holes as well as e) aligned and f) staggered triangular micro-posts, and g) aligned and h) staggered triangular micro-holes. The solid (no-slip) surfaces are illustrated in white color.

3.3. Overall thermal performance of SHS

Although SHSs can curtail the pressure drop through microchannels, they also lead to lower heat transfer rate in comparison to that over conventional surfaces of microchannels. This means that the effect of SHSs should be considered simultaneously when it comes to the applications and significance of SHS in thermal issues. Therefore, a microchannel with the maximum heat transfer and minimum pressure drop is desirable.

For comparison between thermal and hydrodynamic aspects of SHS, goodness factor can be defined as [56]:

$$\varphi = \frac{NuPr^{-1/3}}{fRe}, \tag{10}$$

in which, Prandtl number is represented by Pr. This parameter is constant for a fully developed laminar flow with a specific wall heat flux within parallel plate and equal to

$$\varphi_c = \frac{8.235 \times 7.56^{-1/3}}{96}. \tag{11}$$

Considering this value as a reference, a thermal performance index can be defined as the ratio of φ/φ_c for overall thermal assessment of SHS, expressed by [57]:

$$\eta = \frac{\varphi}{\varphi_c} = \frac{(Nu/fRe)}{(8.235/96)}. \tag{12}$$

This index is compared and shown for alternative microstructures and Reynolds numbers at different cavity fraction in Fig. 14. The upgraded thermal performance can be seen when $\varphi/\varphi_c > 1$ in comparison with the conventional microchannel at the same pumping energy utilization [47]. The interesting point is that the thermal performance indices of triangular configurations are always higher than unity indicating the preeminence of this SHS over a smooth microchannel. Generally, this parameter increases by the rise of Reynolds number and cavity fraction for all geometries. Also, the increment of Reynolds number leads to the higher value of the index for all investigated cases. However, the smooth microchannels are more advantageous than square structures at small values of Re and F_c as the values of thermal indices become less than unity.

The staggered square micro-hole shows its superiority at lower Reynolds numbers while the staggered square posts tend to have a better overall performance at larger Re. Although staggered square hole and posts demonstrate the highest values of goodness factor at low Re, they are aligned triangular hole and staggered square posts that represent the best performance at higher Re. The smallest overall performance is devoted to the aligned square holes and posts. The η graphs imply that the lowest ratio of goodness factor belongs to the aligned square micro-holes and micro-posts, although the chief impact of displacing the microstructures from aligned to staggered applies to these two patterns.

In most cases with triangular geometries, displacing microstructures makes considerable differences except at higher Re and $F_c = 0.9$. Nonetheless, as the heat transfer at low Reynolds number is weak, generally, higher values of Re are applied for cooling purposes. Overall, the rise of cavity fraction triggers the lower values of Nusselt number but a higher value of thermal index. This is since the reduction rate of pressure through the microchannel is more significant than that of heat transfer through walls, in other words, the effect of shear-free interface on drag reduction is more dominant than the decrement of heat transfer resulting in higher overall thermal performance of SHSs.

The use of goodness factor provides a rigorous way of optimizing the design. In case of using these patterned microchannels, the application and circumstances are of great importance. This means that if the drag reduction is of more importance than thermal performance of SHS, then the microchannel with aligned square micro-posts is an ideal selection requiring the lowest power for pumping the fluid through the microchannel. Yet, triangular holes as well as staggered square holes are ideal for enhancing heat transfer at low and high Reynolds numbers, respectively. Further, staggered square holes and posts are the top choices considering overall performance of the patterned microchannels.

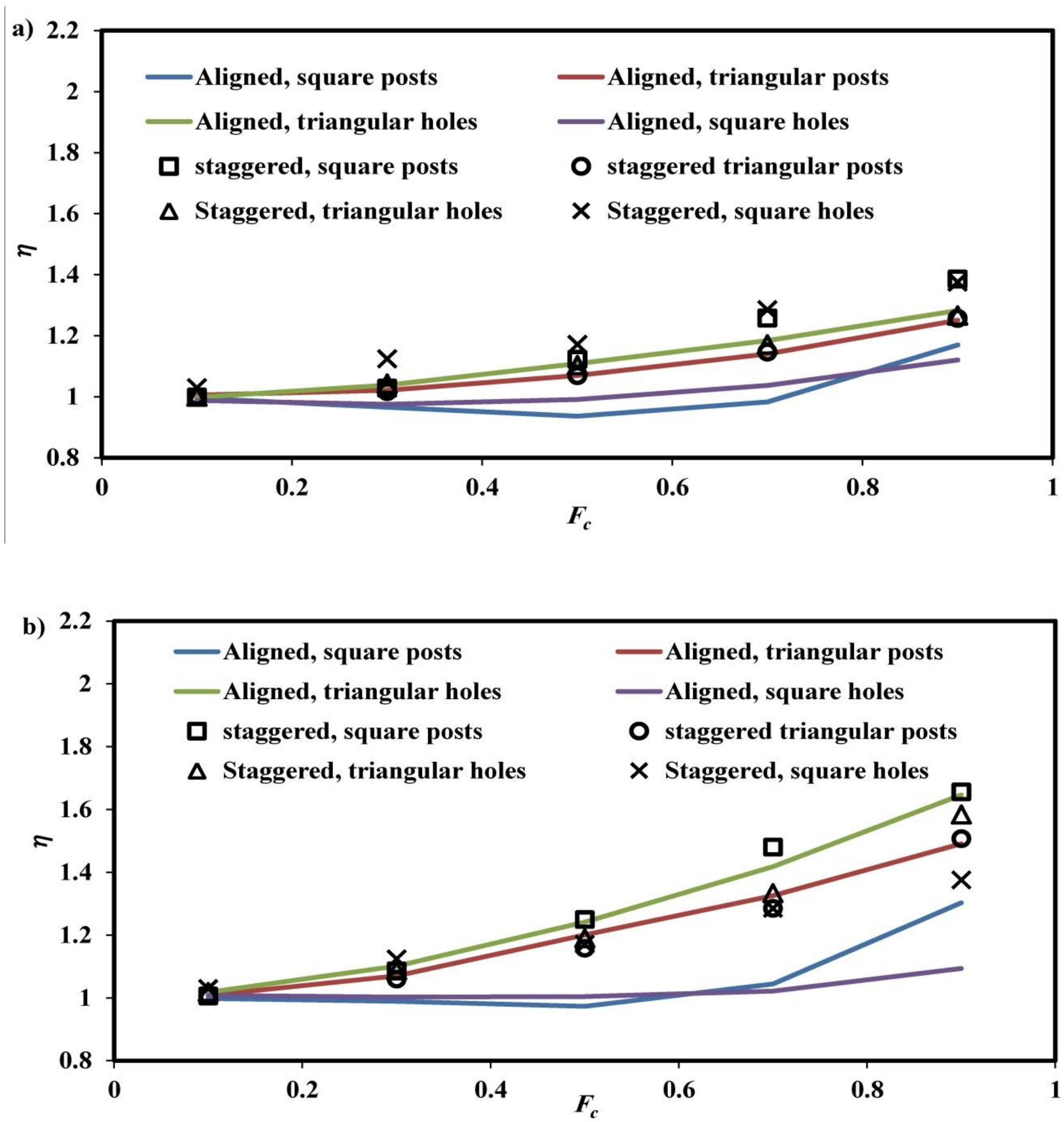

Fig. 14. Impacts of cavity fraction on thermal performance index for different patterns at a) $Re = 10$ b) $Re = 100$.

4. Conclusions

The use of SHSs with triangular microstructures for enhancing the performance of microchannels has so far received limited attention. To address this issue, microchannels with superhydrophobic surfaces consisting of square and triangular micro-posts and micro-holes were investigated numerically in a fully developed laminar flow. The impacts of cavity fractions, Reynolds numbers and various patterns were examined through evaluating the overall thermal performance, Poiseuille and Nusselt number of the microchannel. The key outcomes of this study are summarized in the followings.

- The rise of cavity fraction leads to the decline of the required pumping power and Nusselt numbers. Yet, the thermal performance index, as the simultaneous indicator of hydraulic and thermal performances, increases.
- At low Reynolds numbers and cavity fractions, the effect of SHSs is negligible and the system tends to behave like a conventional microchannel with smooth walls. However, the significant influences of SHS can be clearly seen at higher Re and F_c.
- By escalation of cavity fraction, total shear stress and heat transfer over the microchannel wall diminish while the local values surge.
- Triangular micro-posts and -holes configurations have the maximum heat transfer rates at the low and high cavity fractions for all Re respectively.
- The largest goodness factor ratio is attainable at high values of Reynolds number and cavity fraction, specifically, with patterns of staggered square holes and post at low and high values of Reynolds number.
- Triangular patterns have the best heat transfer performance. Triangular microstructures can be beneficial for all Reynolds numbers and cavity fractions when the total performance of microchannel is concerned. This is because the effect of shear-free interface on drag reduction is more dominant than the decrement of heat transfer for triangular patterns.

- **References**

[1] H.J. Xu, Thermal transport in microchannels partially filled with micro-porous media involving flow inertia, flow/thermal slips, thermal non-equilibrium and thermal asymmetry, Int. Commun. Heat Mass Transf. 110 (2020) 104404. doi:10.1016/J.ICHEATMASSTRANSFER.2019.104404.

[2] A. Bartwal, A. Gautam, M. Kumar, C.K. Mangrulkar, S. Chamoli, Thermal performance intensification of a circular heat exchanger tube integrated with compound circular ring–metal wire net inserts, Chem. Eng. Process. - Process Intensif. 124 (2018) 50–70. doi:10.1016/J.CEP.2017.12.002.

[3] S. Chamoli, R. Lu, P. Yu, Thermal characteristic of a turbulent flow through a circular tube fitted with perforated vortex generator inserts, Appl. Therm. Eng. 121 (2017) 1117–1134. doi:10.1016/J.APPLTHERMALENG.2017.03.145.

[4] S. Chamoli, R. Lu, J. Xie, P. Yu, Numerical study on flow structure and heat transfer in a circular tube integrated with novel anchor shaped inserts, Appl. Therm. Eng. 135 (2018) 304–324. doi:10.1016/J.APPLTHERMALENG.2018.02.052.

[5] S.K. Singh, M. Kumar, A. Kumar, A. Gautam, S. Chamoli, Thermal and friction characteristics of a circular tube fitted with perforated hollow circular cylinder inserts, Appl. Therm. Eng. 130 (2018) 230–241. doi:10.1016/J.APPLTHERMALENG.2017.10.090.

[6] S. Chamoli, P. Yu, S. Yu, Multi-objective shape optimization of a heat exchanger tube fitted with compound inserts, Appl. Therm. Eng. 117 (2017) 708–724. doi:10.1016/J.APPLTHERMALENG.2017.02.047.

[7] S. Chamoli, R. Lu, H. Chen, Y. Cheng, P. Yu, Numerical optimization of design parameters for a modified double-layer microchannel heat sink, Int. J. Heat Mass Transf. 138 (2019) 373–389. doi:10.1016/J.IJHEATMASSTRANSFER.2019.04.032.

[8] J.S. Sawhney, R. Maithani, S. Chamoli, Experimental investigation of heat transfer and friction factor characteristics of solar air heater using wavy delta winglets, Appl. Therm. Eng. 117 (2017) 740–751.

[9] S. Chamoli, R. Lu, D. Xu, P. Yu, Thermal performance improvement of a solar air heater fitted with winglet vortex generators, Sol. Energy. 159 (2018) 966–983. doi:10.1016/J.SOLENER.2017.11.046.

[10] S.G. Kandlikar, M.R. King, Chapter 1 - Introduction, in: S.G. Kandlikar, S. Garimella, D. Li, S. Colin, M.R.B.T.-H.T. and F.F. in M. and M. (Second E. King (Eds.), Butterworth-Heinemann, Oxford, 2014: pp. 1–9. doi:https://doi.org/10.1016/B978-0-08-098346-2.00001-6.

[11] Y. Si, Z. Dong, L. Jiang, Bioinspired designs of superhydrophobic and superhydrophilic materials, ACS Cent. Sci. 4 (2018) 1102–1112.

[12] P. Dimitrakellis, E. Gogolides, Hydrophobic and superhydrophobic surfaces fabricated using atmospheric pressure cold plasma technology: A review, Adv. Colloid Interface Sci. 254 (2018) 1–21.

[13] D.K. Sharma, V. Baghel, R. Kumar, D.K. Avasthi, B.S. Sikarwar, Recent Developments in Fabrication of Super-Hydrophobic Surfaces: A Review, in: Adv. Ind. Prod. Eng., Springer, 2019: pp. 127–140.

[14] E. Vazirinasab, R. Jafari, G. Momen, Application of superhydrophobic coatings as a corrosion barrier: A review, Surf. Coatings Technol. 341 (2018) 40–56.

[15] S.K. Sethi, G. Manik, Recent progress in super hydrophobic/hydrophilic self-cleaning surfaces for various

industrial applications: a review, Polym. Plast. Technol. Eng. 57 (2018) 1932–1952.

[16] K. Manoharan, S. Bhattacharya, Superhydrophobic surfaces review: Functional application, fabrication techniques and limitations, J. Micromanufacturing. 2 (2019) 59–78.

[17] J. Jeevahan, M. Chandrasekaran, G.B. Joseph, R.B. Durairaj, G. Mageshwaran, Superhydrophobic surfaces: a review on fundamentals, applications, and challenges, J. Coatings Technol. Res. 15 (2018) 231–250.

[18] P. Marc, C. Steven, Mitigation of hydrodynamic resistance: Methods to reduce hydrodynamic drag, World Scientific, 2014.

[19] Y. Zhu, H.K. Mutha, Y. Zhao, E.N. Wang, Manipulating Water and Heat with Nanoengineered Surfaces BT - Women in Nanotechnology: Contributions from the Atomic Level and Up, in: P.M. Norris, L.E. Friedersdorf (Eds.), Springer International Publishing, Cham, 2020: pp. 85–99. doi:10.1007/978-3-030-19951-7_7.

[20] A.B.D. Cassie, Discussions of the Faraday Society, Faraday Soc. 3 (1948) 11–16.

[21] R.N. Wenzel, Ind Eng Chem 1936, 28, 988;(g) Wenzel, RN J Phys Colloid Chem. 53 (1949) 1466.

[22] J. Ou, B. Perot, J.P. Rothstein, Laminar drag reduction in microchannels using ultrahydrophobic surfaces, Phys. Fluids. 16 (2004) 4635–4643.

[23] J. Ou, J.P. Rothstein, Direct velocity measurements of the flow past drag-reducing ultrahydrophobic surfaces, Phys. Fluids. 17 (2005) 103606.

[24] D. Maynes, K. Jeffs, B. Woolford, B.W. Webb, Laminar flow in a microchannel with hydrophobic surface patterned microribs oriented parallel to the flow direction, Phys. Fluids. 19 (2007) 93603.

[25] C.J. Teo, B.C. Khoo, Analysis of Stokes flow in microchannels with superhydrophobic surfaces containing a periodic array of micro-grooves, Microfluid. Nanofluidics. 7 (2009) 353.

[26] A. Cowley, D. Maynes, J. Crockett, Inertial effects on thermal transport in superhydrophobic microchannels, Int. J. Heat Mass Transf. 101 (2016) 121–132.

[27] M.H. Sotoude Haghighi, S.M. Mirghavami, M.M. Ghorani, A. Riasi, S.F. Chini, A numerical study on the performance of a superhydrophobic coated very low head (VLH) axial hydraulic turbine using entropy generation method, Renew. Energy. 147 (2020) 409–422. doi:10.1016/J.RENENE.2019.09.003.

[28] D.V. Krishnan, G.U. Kumar, S. Suresh, M. Jubal, M.R. Thansekhar, R. Ramesh, Wetting transition in laser-fabricated hierarchical surface structures and its impact on condensation heat transfer characteristics, Int. J. Heat Mass Transf. 140 (2019) 886–896.

[29] S. Wang, X. Yu, C. Liang, Y. Zhang, Enhanced condensation heat transfer in air-conditioner heat exchanger using superhydrophobic foils, Appl. Therm. Eng. 137 (2018) 758–766.

[30] W. Choi, H. Byeon, J.Y. Park, I.C. Kim, S.J. Lee, Effects of pressure gradient on stability and drag reduction of superhydrophobic surfaces, Appl. Phys. Lett. 114 (2019) 101603.

[31] N. Norouzi, A.A. Gharehaghaji, M. Montazer, Reducing drag force on polyester fabric through superhydrophobic surface via nano-pretreatment and water repellent finishing, J. Text. Inst. 109 (2018) 92–97.

[32] Y. Tuo, H. Zhang, W. Rong, S. Jiang, W. Chen, X. Liu, Drag Reduction of Anisotropic Superhydrophobic Surfaces Prepared by Laser Etching, Langmuir. 35 (2019) 11016–11022.

[33] Y. Tuo, W. Chen, H. Zhang, P. Li, X. Liu, One-step hydrothermal method to fabricate drag reduction superhydrophobic surface on aluminum foil, Appl. Surf. Sci. 446 (2018) 230–235.

[34] A. Rastegari, R. Akhavan, On drag reduction scaling and sustainability bounds of superhydrophobic surfaces in high Reynolds number turbulent flows, J. Fluid Mech. 864 (2019) 327–347.

[35] A. Rajappan, K. Golovin, B. Tobelmann, V. Pillutla, Abhijeet, W. Choi, A. Tuteja, G.H. McKinley, Influence of textural statistics on drag reduction by scalable, randomly rough superhydrophobic surfaces in turbulent flow, Phys. Fluids. 31 (2019) 42107.

[36] R.A. Bidkar, L. Leblanc, A.J. Kulkarni, V. Bahadur, S.L. Ceccio, M. Perlin, Skin-friction drag reduction in the turbulent regime using random-textured hydrophobic surfaces, Phys. Fluids. 26 (2014) 85108.

[37] J.W. Gose, K. Golovin, M. Boban, J.M. Mabry, A. Tuteja, M. Perlin, S.L. Ceccio, Characterization of superhydrophobic surfaces for drag reduction in turbulent flow, J. Fluid Mech. 845 (2018) 560–580.

[38] H.J. Xu, Z.B. Xing, F.Q. Wang, Z.M. Cheng, Review on heat conduction, heat convection, thermal radiation and phase change heat transfer of nanofluids in porous media: Fundamentals and applications, Chem. Eng. Sci. 195 (2019) 462–483. doi:10.1016/J.CES.2018.09.045.

[39] R. Enright, M. Hodes, T.R. Salamon, Y. Muzychka, Analysis and simulation of heat transfer in a superhydrophobic microchannel, in: 2010 14th Int. Heat Transf. Conf., American Society of Mechanical Engineers Digital Collection, 2011: pp. 157–168.

[40] M. Kharati-Koopaee, M.R. Akhtari, Numerical study of fluid flow and heat transfer phenomenon within microchannels comprising different superhydrophobic structures, Int. J. Therm. Sci. (2018). doi:10.1016/j.ijthermalsci.2017.11.004.

[41] A. Amin, Three-dimensional numerical simulations of liquid laminar flow over superhydrophobic surfaces with post geometries, (2011).

[42] C.-O. Ng, C.Y. Wang, Temperature jump coefficient for superhydrophobic surfaces, J. Heat Transfer. 136 (2014) 64501.

[43] C.J. Teo, B.C. Khoo, Effects of interface curvature on Poiseuille flow through microchannels and microtubes containing superhydrophobic surfaces with transverse grooves and ribs, Microfluid. Nanofluidics. 17 (2014) 891–905.

[44] D. Maynes, J. Crockett, Apparent temperature jump and thermal transport in channels with streamwise rib and cavity featured superhydrophobic walls at constant heat flux, J. Heat Transfer. 136 (2014) 11701.

[45] D. Maynes, B.W. Webb, J. Crockett, V. Solovjov, Analysis of laminar slip-flow thermal transport in microchannels with transverse rib and cavity structured superhydrophobic walls at constant heat flux, J. Heat Transfer. 135 (2013) 21701.

[46] H. Ryu, J. Kim, J. Kim, D.H. Kim, Y.-J. Kang, Y.-J. Jang, J.H. Jeong, Enhancement of a heat transfer performance on the Al6061 surface using microstructures and fluorine-doped diamond-like carbon (F-DLC) coating, Int. J. Heat Mass Transf. 148 (2020) 119108. doi:https://doi.org/10.1016/j.ijheatmasstransfer.2019.119108.

[47] Y. Cheng, J. Xu, Y. Sui, Numerical study on drag reduction and heat transfer enhancement in microchannels

with superhydrophobic surfaces for electronic cooling, Appl. Therm. Eng. 88 (2015) 71–81.

[48] A. Cowley, D. Maynes, J. Crockett, Effective temperature jump length and influence of axial conduction for thermal transport in superhydrophobic channels, Int. J. Heat Mass Transf. 79 (2014) 573–583. doi:10.1016/J.IJHEATMASSTRANSFER.2014.08.033.

[49] R. Enright, M. Hodes, T. Salamon, Y. Muzychka, Isoflux Nusselt number and slip length formulae for superhydrophobic microchannels, J. Heat Transfer. 136 (2014) 12402.

[50] B.L. Woolford, Laminar and turbulent flow of a liquid through channels with superhydrophobic walls exhibiting alternating ribs and cavities, (2009).

[51] C.-O. Ng, C.Y. Wang, Apparent slip arising from Stokes shear flow over a bidimensional patterned surface, Microfluid. Nanofluidics. 8 (2010) 361–371.

[52] M. Liravi, H. Pakzad, A. Moosavi, A. Nouri-Borujerdi, A comprehensive review on recent advances in superhydrophobic surfaces and their applications for drag reduction, Prog. Org. Coatings. 140 (2020) 105537.

[53] M.A. Samaha, H.V. Tafreshi, M. Gad-el-Hak, Effects of hydrostatic pressure on the drag reduction of submerged aerogel-particle coatings, Colloids Surfaces A Physicochem. Eng. Asp. 399 (2012) 62–70.

[54] C. Ybert, C. Barentin, C. Cottin-Bizonne, P. Joseph, L. Bocquet, Achieving large slip with superhydrophobic surfaces: Scaling laws for generic geometries, Phys. Fluids. 19 (2007) 123601.

[55] C.F. Carlborg, W. van der Wijngaart, Sustained superhydrophobic friction reduction at high liquid pressures and large flows, Langmuir. 27 (2010) 487–493.

[56] B. Zohuri, Compact heat exchangers, Springer, 2017.

[57] D. Maynes, B.W. Webb, J. Davies, Thermal transport in a microchannel exhibiting ultrahydrophobic microribs maintained at constant temperature, J. Heat Transfer. 130 (2008) 22402.